Remote Magnetic Microengineering and Alignment of Spheroids into 3D Cellular Fibers

Noam Demri, Simon Dumas, Manh-louis Nguyen, Giacomo Gropplero, Ali Abou-Hassan, Stéphanie Descroix, Claire Wilhelm

Remote magnetic microengineering and alignment of spheroids into 3D cellular fibers

Noam Demri, Simon Dumas, Manh-Louis Nguyen, Giacomo Gropplero, Ali Abou-Hassan, Stéphanie Descroix, and Claire Wilhelm**

N. Demri, S. Dumas, M-L. Nguyen, G. Gropplero, S. Descroix, C. Wilhelm

Laboratoire Physico Chimie Curie, PCC, CNRS UMR168, Institut Curie, Sorbonne University, PSL University, 75005 Paris, France.

E-mails: stephanie.descroix@curie.fr, claire.wilhelm@curie.fr;

A. Abou-Hassan

PHysico-chimie des Electrolytes et Nanosystèmes InterfaciauX, PHENIX, CNRS UMR234, Sorbonne University, 75005 Paris, France.

Keywords: magnetic nanoparticles, magnetic forces, muscle tissue engineering, spheroids, organ on chip, 3D cell culture

Developing *in vitro* models that recapitulate the *in vivo* organization of living cells in a 3D microenvironment is one of the current challenges in the field of tissue engineering. In particular for anisotropic tissues where alignment of precursor cells is required for them to create functional structures. Herein, we propose a new method that allows aligning in the direction of a uniform magnetic field both individual cells (muscle, stromal and stem cells) or spheroids in a thermoresponsive collagen hydrogel. In an all-in-one approach, spheroids are generated at high throughput by magnetic engineering using microfabricated micromagnets and are used as building blocks to create 3D anisotropic tissue structures of different scales. The magnetic cells and spheroids alignment process is optimized in terms of magnetic cell labelling, concentration, and size. Anisotropic structures are induced to form fibers in the direction of the magnetic alignment, with the respective roles of the magnetic field, the mechanical stretching of hydrogel or co-cultivating of the aligned cells with non-magnetic stromal cells, being investigated. Over days, spheroids fuse into 3D tubular structures, oriented in the direction of the magnetic alignment. Moreover, in the case of the muscle cells model, multinucleated cells can be observed within the fibers.

1. Introduction

In various research fields including life sciences, translational research and clinics, the development of *in vitro* cell culture models that faithfully recapitulate *in vivo* complexity remains a cornerstone. It is now admitted that 2D cell culture approaches differ from physiological or pathophysiological conditions in particular regarding cell-cell and cell-matrix interactions. In this context, organ on chip technology has emerged as a solution to mimic *in vivo* complexity, and to offer control of the cellular microenvironment. More specifically, these micro-physiological systems offer the possibility to co-culture different cell types in 3D extracellular matrix to recapitulate organ features and functions as best as possible. Over the past decade, the field of organ on chips has markedly expanded, with various technological approaches being proposed to recapitulate many different organs in microfluidic devices.[1] These micro-devices offer an unprecedented level of control, provide a unique opportunity to better understand how function and structure are intimately linked, and can focus on a single organ or even mimic organisms with multi-organ platforms.[2] Yet, they rely mostly on 3D scaffold to self-organize cells within. There is now a need to better control cell positioning in on-chip 3D extracellular matrix to better mimic *in vivo* 3D tissue organization.

For instance, one hallmark of muscle tissue is the spatial alignment of the component cells. The parallel arrangement of cardiomyocytes or skeletal muscle myofibers is necessary for efficient electromechanical coupling, electrical anisotropy and directional contractile force generation.[3] Bioengineered muscle constructs must therefore contain muscle cells densely packed in a 3D structure, and amenable to alignment with one another in a preferential direction.[4] Most attempts to align muscle cells have been achieved by taking advantage of the substrate anisotropy and/or topography,[5] for example, using nanofibers[6] or micropatterning.[7] Cell alignment within a 3D engineered tissue construct remains a challenge. One solution consisted of orienting muscle cells by anchoring them between two posts that guide 3D cell alignment.[8]

To orient cells within a 3D scaffold, one possibility is to manipulate them remotely to make them interact and self-organize. To achieve this, magnetic forces acting at a distance are appealing candidates, provided the cells are first rendered magnetic. The idea is then to take advantage of magnetic nanoparticles (NPs), already exploited for theranostics applications as contrast agents for magnetic resonance imaging or as heat mediators in photothermal or/and magnetic hyperthermia therapies.[9] The strategy of using cells loaded with magnetic nanoparticles for cell manipulation and tissue engineering is more recent.[10] It was initially pioneered with the concept of magnetic sheet engineering,[11] allowing tissue formation via

successive cell layering in the presence of a magnetic field gradient. Magnetic forces have next been further exploited for controlled tissue assembly,[12] to create cell spheroids,[13] towards 3D tissue engineered structures,[14] with the possibility for in situ magneto-mechanical stimulation.[15]

Among the existing methods for 3D cell culture, one of the most popular approaches remains spheroids. Spheroids offer multiple advantages as they allow high cell cohesion and facilitate handling of the cell constructs with conventional equipment. Though often advantageous, spheroids do not offer the same level of complexity as *in vivo* tissue in terms of spatial organization, and do not allow the implementation of external forces or tissue deformation. In recent studies, spheroids have been used as building blocks to recreate complex *in vivo*-like structural organization.[16] Many of these methods rely on bioprinting, where the spheroids are mixed with a hydrogel scaffold to make a bioink, which is then extruded on a surface before polymerization.[17] Most current spheroids production methods, including the magnetic-based ones, still suffer from poor spatial control over spheroids, from large diameter over 100 μm , or/and from low number of spheroids produced.

In this context,[18] we propose a multiscale magnetic approach for anisotropic tissue engineering, that is based on the high-throughput production of size-controlled magnetic spheroids with diameter in the 50-100 μm range.

Based on an optimized cell labeling protocol by iron-oxide NPs, we started by developing a magnetic method to form size-controlled spheroids using magnetic micro-patterns. We then exploited the magnetic dipolar forces created in between magnetic individual cells or spheroids by a uniform magnetic field to act as a “compass” and create preferential alignment of either single cells or spheroids. This magnetic alignment was achieved in a 3D scaffold made of a mixture of collagen I and Matrigel, that could additionally be mechanically stretched thanks to a specific microfluidic chip design or co-cultured with stromal cells. The method was initially developed using muscle cells, leading to the formation of cohesive muscle cell fibers, but was also demonstrated to work with stromal and mesenchymal stem cells, illustrating its versatility.

2. Results and Discussion

2.1. Internalization of magnetic nanoparticles (NPs) in cells

The cellular magnetic labeling was developed with muscle C2C12 cells, using citrate-coated iron oxide NPs (8 nm in diameter). These negatively charged nanoparticles are internalized in

cells following the endocytotic pathway, and concentrate within endosomes, where they are slowly degraded over time, while the iron released integrates the iron cellular metabolism and is stored within ferritin.[19] Herein, different magnetic labeling conditions were investigated with the goal to determine non-harmful conditions with high intracellular magnetic NPs content. This was done by varying iron concentration (ranging from 1 to 32 mM) and incubation time (from 15 min to 16 h). The amount of NPs internalized by cells was assessed by single cell magnetophoresis while the effect of NP internalization on cell viability was measured by resazurin-based metabolic test.

As expected, cells internalized more NPs when increasing incubation time or NP concentration in the labeling solution (**Figure 1**). For a magnetic labeling performed at a constant iron concentration of 2 mM and by varying incubation time, we observed a saturation reached for incubations longer than 4 hours (Figure 1A). Similarly, at a given incubation time of 30 min, the NPs internalization increases with the iron concentration, and rapidly reaches a plateau above 8 mM (Figure 1B). Interestingly, cell viability was reduced in a dose dependent manner (Figure 1A and Figure 1B), either for incubation times longer than 2h (at 2 mM of iron) or for iron concentrations above 8 mM (30 min duration). These results suggest that the maximum level of NPs internalized by cells without impacting cells metabolic activity is about 10 pg per cell. To further increase this level, we developed and evaluated the potential of a multistep sequential labeling (Figure 1C): C2C12 cells were incubated for 30 min with 2 mM of iron on consecutive days, with one incubation a day, with up to 3 days of incubation (referred to as NP1, NP2 and NP3 according to the number of consecutive incubations). This sequential magnetic labeling allowed internalizing twice or three times as much NPs per cell as with single step labeling procedures, while perfectly preserving the cells metabolic activity. Altogether, these results evidenced that the use of sequential magnetic labeling provides the cells with high NPs internalization, in the range of 20 pg of iron per cell without impacting cells metabolic activity. This suggests that rather than the overall amount of iron internalized, it is the internalization rate that has more impact on the cells metabolic activity. In addition to the metabolic activity assays, the impact of the NP1, NP2 and NP3 labeling conditions on cell viability was tested using a Live/Dead assay. The proportion of dead cells was 0.7±0.5% for the non-labeled control cells, and was found at 0.9±0.8%, 1±0.6%, and 0.5±0.3% (n=3) for NP1, NP2, and NP3 labeling conditions, respectively, showing no significant impact on cell viability. Next step was to investigate the NP3 high content magnetic labeling on the muscle cells differentiation. To do so, magnetically labeled cells were grown in 2D cell culture in a medium promoting differentiation. Cell differentiation was evidenced by histological,

confocal, and electron microscopy imaging, characterized by the fusion of several muscle precursor cells into muscle fibers.[20] Figures 1D-1H show that after 8 days of culture magnetically labeled cells fuse to form large myofibers. In addition, both the histological (Perls) and electron microscopy imaging localize the NPs inside the cells, within endosomes, either right after labeling (day 0) or after the differentiation process (day 8 or day 12). All observations converge towards the presence of multinucleated cells, that are clearly detected by confocal (Figure 1F) or electron microscopy imaging (Figure 1H), confirming qualitatively that the magnetic labeling of muscle cells does not impede the first stages of their differentiation. Further investigations would require to evaluate quantitatively the impact of nanoparticles on muscle differentiation by real-time qPCR.

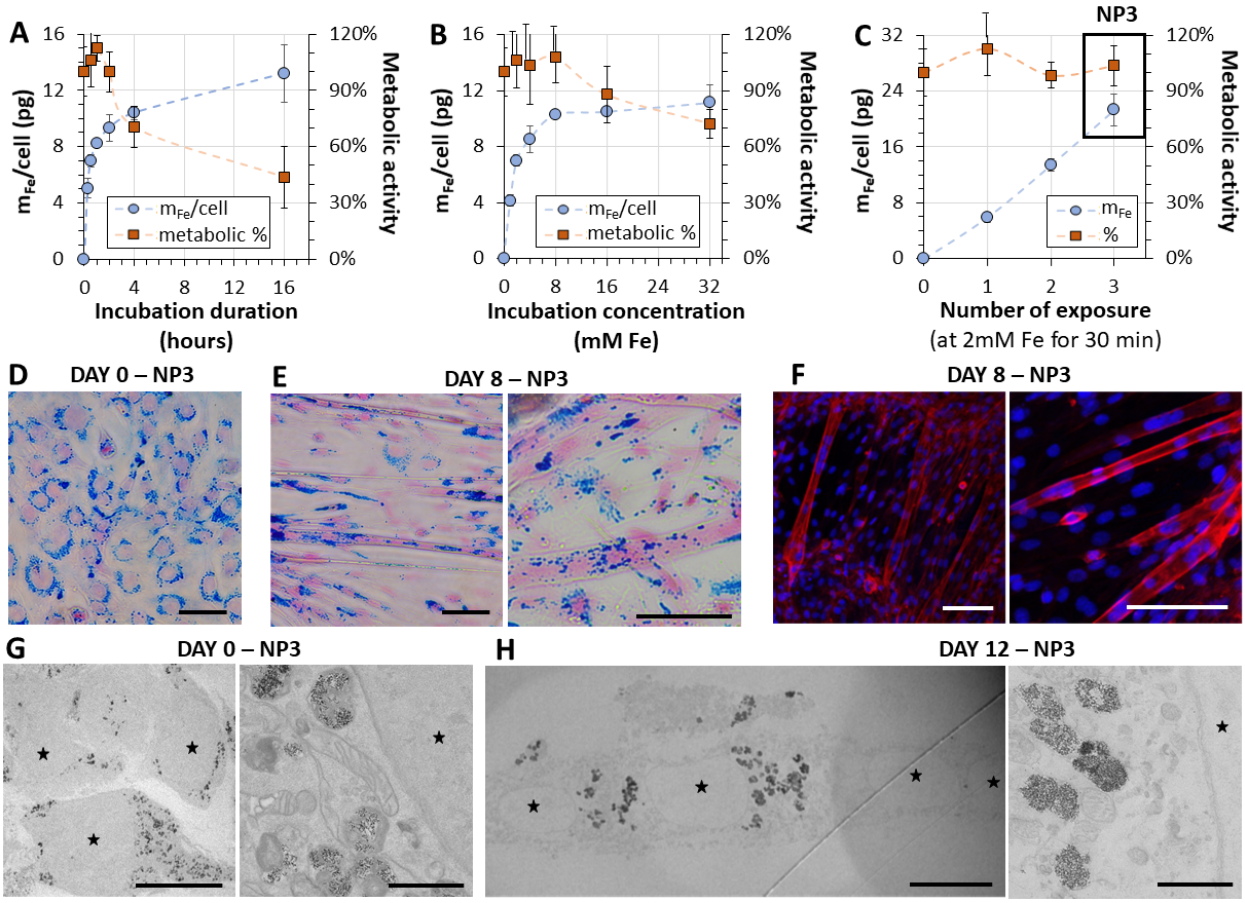

Figure 1. (A-C) Quantification of magnetic nanoparticles internalization in cells measured by magnetophoresis and cell metabolic activity after labeling measured with Alamar Blue reagent. (A): Incubation at [Fe] = 2 mM for durations ranging from 15mn to 16h, (B): Incubation for 30 min with concentration of iron ranging from 1 to 32 mM, (C): Incubation at 2 mM for 30 min, once a day, for 1 (NP1 labeling), 2 (NP2 labeling) or 3 (NP3 labeling) consecutive days. Magnetophoresis was performed on 200 cells per condition and data are shown as the mean ± standard deviation (SD). (D): Perls iron blue staining counterstained with Nuclear fast red, for cells labeled in NP3 condition, right after labeling (day 0). (E): Perls staining of cells after 8 days of differentiation (2D cell culture). Scale bars = 100 µm (F):

Confocal imaging of cells after 8 days of differentiation, with the actin stained in red and nuclei in blue. Scale bars = 100 µm (G,H): Transmission electron microscopy of cells labeled with NP3, after labeling (G, day 0) or left differentiating on a 2D surface for 12 days (H), which shows endosomes filled with nanoparticles in both cases and cells with several nuclei (each nucleus is indicated with a star) upon differentiation. Scale bars = 10 µm (left image) and 1 µm (right image).

2.2. Magnetic field configuration for magnetic cell alignment in 3D microenvironment

To further develop a muscle on chip model based on magnetic cell positioning, we investigated how magnetic forces can be exploited to align on chip magnetized cells in a 3D hydrogel scaffold serving as an extra-cellular matrix (ECM). The principle of magnetic alignment is illustrated in **Figure 2**. Collagen I being the most abundant protein of muscle ECM, a mixture of collagen I (2 mg mL^{-1}) and Matrigel (10% v/v) was used to provide cells with a 3D scaffold. This scaffold solution was mixed with the magnetically labeled cells and poured into a glutaraldehyde treated PDMS chip. The glutaraldehyde treatment was necessary to covalently graft collagen to PDMS, preventing collagen detachment due to forces exerted by muscle cells. To study cell response to a magnetic field in a 3D hydrogel, the chips were placed in between two magnets for 30 min at 37°C, to trigger cell alignment before hydrogel polymerization (Figure 2A). Such an alignment is supposed to happen due to magnetic dipole interactions between magnetized cells, each one holding a magnetic moment in the presence and direction of an applied magnetic field.

Magnetic cell alignment yet necessitates an optimized magnetic configuration developing a perfectly uniform magnetic field. Indeed, the challenge here is to avoid any magnetic field gradient that would generate a magnetophoretic mobility of the cells within the chips. To achieve a strong yet uniform magnetic field, the simplest configuration is to face two magnets symmetrically (Figure 2B). The two magnets inter-distance was adjusted using finite-element simulations to minimize the magnetic field gradient in the chamber and avoid magnetic attraction of the cells towards the magnets. As expected, the symmetrical magnets configuration generates a magnetic field with lines perpendicular to the direction of the magnets (Figure 2B). The optimal distance between the magnets that minimizes the magnetic field gradient is achieved at 3.6 cm (Figure 2C). This 3.6 cm inter-magnet distance and a 10 cm one were experimentally tested for magnetic cells alignment. Figure 2D shows that for a distance of 10 cm, even if remarkably aligned, the magnetic cells are not homogeneously distributed along the y-axis of the chamber, most of them migrating towards one of the magnets, which confirms the presence of a magnetic field gradient. In contrast, when using the optimal inter-distance of 3.6 cm, magnetic cells are both aligned along the magnetic field

lines and homogeneously distributed along the y-axis (Figure 2E). In this configuration, the average dipole/dipole force that attracts cells together and make them align is around 25 pN between two cells in contact labeled with NP3. For both conditions, the chips were left for 30 min at 37°C within the magnets, allowing the hydrogel to fully polymerize. After polymerization, the cells can no longer move freely in the gel and are trapped in this aligned configuration, even when removed from the magnets, and then the chip is filled with medium promoting differentiation.

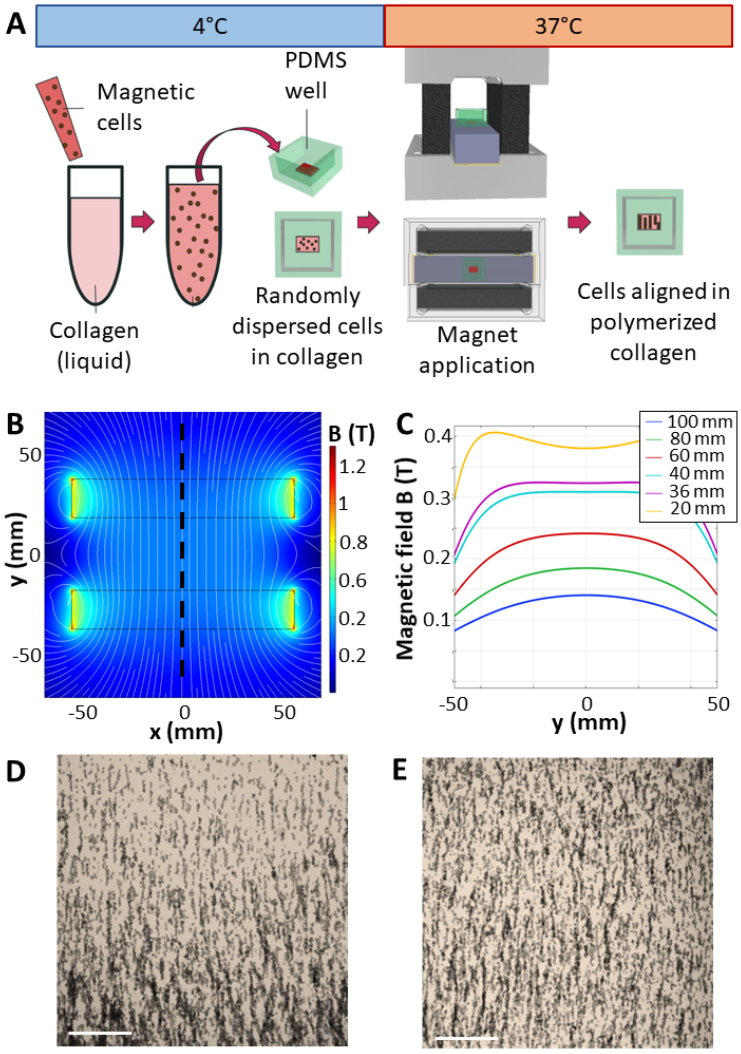

Figure 2. (A): Illustration of the alignment procedure and set-up. (B): Finite elements simulations (COMSOL) of the magnetic field over the z-slice (z=0) passing through the center of the magnets when they are spaced with 3.6 cm. (C): magnetic field over the line (z=x=0) that passes through both magnets' center (in dashes in (B)) for distances between the magnets ranging from 10 to 2 cm. (D): Image of magnetic cell alignment when the magnets are 10 cm apart and the gradient is not optimized showing cells attracted towards the magnets. (E): Images of the magnetic cell alignment when the gradient is optimized with magnets 3.6 cm apart, showing cells chains uniformly distributed. Scale bars = 200 µm. The direction of the magnetic field lines (and subsequent cell alignment) is from top to bottom.

2.3. Magnetic cell alignment varies with cell labeling and concentration

Using this magnetic alignment approach, we were able to form chains made of cells with length ranging from a few tens to hundreds of micrometers (**Figure 3**). Figure 3A shows the effect of cell magnetization on cell alignment. The three labeling protocols - NP1, NP2 and NP3 - were used, consisting in respectively one, two or three consecutive days of cell labeling with an iron concentration of 2 mM during 30 min, and leading to an iron content ranging from 7 pg per cell (NP1) to 20 pg per cell (NP3). Magnetically labeled cells were then seeded in the hydrogel solution at a concentration of 1 million cells per mL, poured at 4°C in the PDMS chips, and rapidly subjected to the magnetic field at 37°C to induce gel polymerization. Figure 3A evidences that for the lower iron content per cell (NP1) cells are barely aligned while for the higher (NP3) most of the cells are organized within distinctive chains, simply mirroring the balance of forces (drag force against dipole-dipole force) experienced by the cells, magnetic dipole-dipole force being proportional to the magnetic cell moment squared, and thus to the quantity of magnetic material within cells (squared as well). As a result, the chain length increases significantly with iron loading, with average values of 59±2 µm, 72±3.5 µm, and 104±12.8 µm for NP1, NP2, and NP3 labeling conditions, respectively (Figure 3D).

The effect of the initial cell concentration on chain formation was next investigated (Figure 3B). As the dipole-dipole force decreases proportionally with the distance between the dipoles to the power of 4, we can expect the distance between cells, and therefore the cell concentration, to be a critical parameter for chain formation. The results show that doubling the cell concentration to 2 million cells/mL with NP3 labeling leads to an increase of the average chain length from 104±12.8 µm to 142.8±8.2 µm (Figure 3D).

The ECM of a skeletal muscle is a dynamic structure which is continuously remodeled by muscle cells but also by stromal cells and in particular fibroblasts, which also play an important role in myogenesis.[21] This complexity must be considered when developing a 3D muscle tissue on chip. To recapitulate this feature, it was important to verify that magnetic alignment could still be achieved in the presence of non-magnetic fibroblasts. Fibroblasts were mixed with the magnetically labeled muscle cells before seeding on the chip. Figure 3C illustrates this co-culture condition, with one cell type (muscle cells) organized anisotropically and the other (fibroblasts) randomly dispersed within the gel. The presence of fibroblasts does not impede muscle cell chain formation but slightly decreases the average value of the chain length, to 93.7±12.8 µm (respective to 104 µm without fibroblast) and 128.2±20.6 µm (142.8

µm without fibroblasts), for 1 million and 2 million muscle cells per mL, respectively (Figure 3D). The 3D magnetic alignment approach can therefore accommodate and co-culture different cell types, both magnetic and non-magnetic, while preserving cell alignment. All conditions are represented in Figure 3D, as boxplots including all chains analyzed (over 2000). It clearly shows an important dispersion of the chain length distribution, with an average polydispersity of 0.9±0.3 over all conditions.

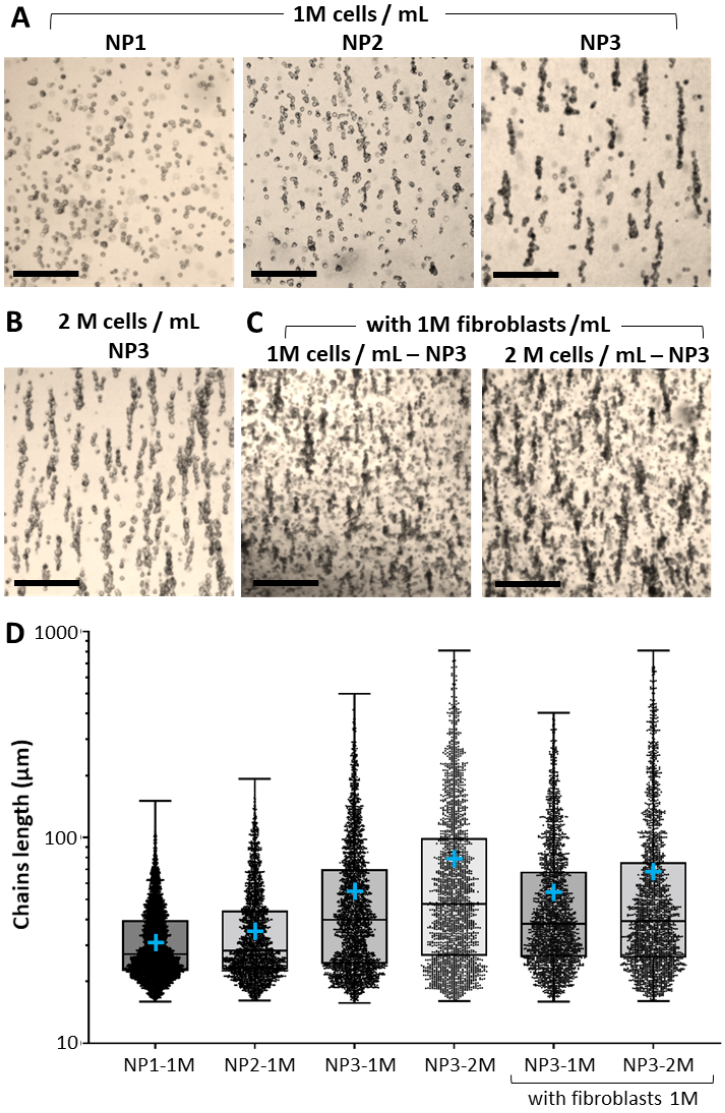

Figure 3. Impact of the magnetic labeling, the cell concentration and co-culture on cell chain length. (1): Images of cells labeled with NP1, NP2 and NP3 and aligned in hydrogel at a concentration of 1 million (1M) cells per mL. (B): Cells labeled with NP3 and aligned at a concentration of 2 million (2M) cells per mL. (C): Cells labeled with NP3 and aligned in hydrogel with 1 million per mL fibroblasts at concentrations of 1 and 2 million per mL magnetic muscle cells. (D): Boxplots of the distributions of chain length for the 6 conditions, showing that the more labeled and the more concentrated the cells are the longer the cell

chains become. Data were obtained over three distinct experiments per condition, with overall more than 2000 chain lengths measured.

2.4. Magnetic cell alignment fades over culture time

We next examined how the cells alignment evolved with time. Already after only one day of culture, muscle cells start colonizing the gel and progressively lose alignment. It is shown in **Figure 4**, within two days of culture, by typical brightfield images, and analysis of the distribution of cell chain angles. In Figure 4A, anisotropy is no longer present, with an almost homogeneous distribution of the angles after two days of culture. To try to preserve this anisotropy, and further promote cell fusion in the chain direction, the chips were maintained in between the magnets during the whole culture (Figure 4C). While many cells were still escaping chaining, the magnetic field partially preserved some cell alignment, with a narrower angle distribution (Figure 4D). After 8 days of culture in differentiation medium, the few cells that maintained their alignment were able to fuse and generate muscle fibers (Figure 4E-F). Overall, these results showed that the magnetic alignment of individual cells for short or extended periods of time is not sufficient to maintain the anisotropy over time, although some cell fusion events can be observed to a limited extent when the magnetic field is maintained all the time.

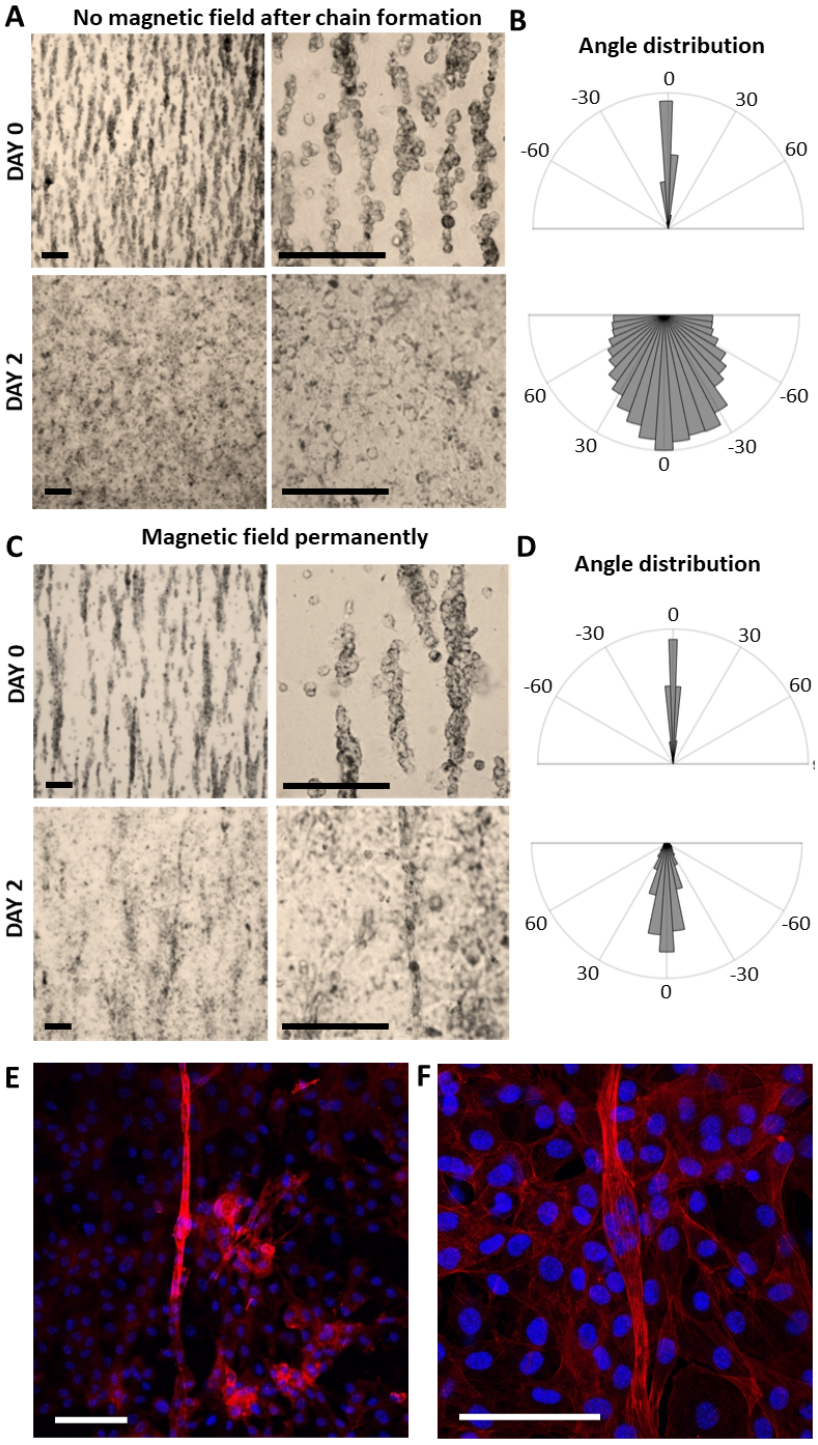

Figure 4. Evolution of the directionality of cell chains over time. (A,B): Condition without magnetic field. (C, D): The chips were kept between the magnets during the whole observation time. (A, C): Images of the cell chains at day 0 and day 2 after cell chain formation. (B, D): Angle distribution within the samples at day 0 and day 2 after cell chain formation. Angle distribution was measured throughout time on 3 distinct samples for each condition. (E,F): Confocal images of samples kept between the magnets all the time; actin stained in red and nuclei in blue, after 8 days of differentiation. Scale bars = 100 µm.

2.5. High-throughput production of magnetic spheroids using micropatterned NiFe attractors

To avoid the almost total loss of anisotropy in the first-aligned muscle cells on chip, we proposed to redesign the alignment method starting with magnetic spheroids instead of individual cells. Indeed, we hypothesize that (i) spheroids provide high cell density and cohesion, that should promote cell-cell interaction and differentiation; (ii) cells being initially trapped within the spheroid, it should prevent the presence of single cells between the chains that would arrange with a random cell density and orientation; and (iii) once aligned one to the other, the spheroids chain already form a pre-muscle structure with the diameter of a myofiber.

Many methods allow producing spheroids including hanging drop arrays, ultra-low attachment wells or magnetic attraction.[13a, 13b, 22] Most of these methods for making spheroids, whether they are magnetic or not, generate at most a few hundreds of spheroids, usually larger than 100µm, and require at least one day of incubation. However, magnetic alignment would actually require several thousand spheroids and they should not be much larger than the diameter of a myofiber. Therefore, herein, we developed a magnetic patterning method to generate rapidly (a few hours) small (below 100 µm) and size-controlled magnetic spheroids at high throughput (**Figure 5**). It is based on a microfabricated array of soft magnetic NiFe (permalloy) micropatterns that can be magnetized by an external magnetic field and generate high magnetic field gradients in their vicinity. Each pattern should thus attract magnetized cells that aggregate and round up into a cohesive spheroid (Figure 5A). The magnetic array was fabricated by combining photolithography and electroplating on glass slides.[23] Two sizes of the NiFe structures were achieved, with a cylindrical shape of 50 µm in height and 50 or 100 µm in diameter, regularly spaced of 100 µm from each other (Figure 5B). To ensure biocompatibility and avoid cell adhesion on the substrate, the magnetic patterns were spin-coated with PDMS and treated with anti-adhesive solution prior to each spheroid production. Magnetic cells were thus directly put in contact with the patterns, at a density of 35, 70, and 140 cells per single micropattern. The magnetic field gradient was calculated through finite-element simulations in 3D using COMSOL Multiphysics 5.5 (Magnetic Field No Currents module). The magnetic properties of the materials were set as follows: a remanent flux density of 1.35 T for the permanent magnets, a permalloy (80Ni:20Fe) magnetization curve for the micromagnets, and non-interacting ($\mu r = 0$) for other surrounding volume (PDMS, glass, air). The magnetic field gradient was extracted on a horizontal line 50 µm above the Ni-patterned surface. It showed that the magnetic field

gradient varies between 300 and 600 T/m, respectively at the center and at the edge of the pattern. For an NP3-labeled cell (21 pg of iron per cell, equivalent to a magnetic moment at saturation of $1.7x10^{-12}$A.m²), this leads to an average attraction force in between 0.5 and 1 nN. 3 hours of aggregation were then sufficient to generate cohesive spheroids on top of each micromagnet (Figure 5C), that can be further collected. The first observation was that using micromagnets of 50 µm or 100 µm in diameter did not change the size of the resulting spheroids as long as the number of cells per pattern was identical. The impact of cell concentration (35, 70, and 140 cells per pattern) and magnetic labeling (NP1, NP2, and NP3 conditions) was next examined. The higher the initial cell concentration, the larger the magnetic spheroids (Figure 5D): with the NP3 labeling condition, concentrations of 35 and 140 cells per pattern resulted in spheroids of 57±1 µm and 97±1 µm in diameter, respectively (Figure 5E). Similarly, the higher the magnetic labeling, the larger the spheroids: spheroids generated with NP1, NP2 and NP3 labeled cells present an average diameter of 64±1, 74±2 and 97±1 µm, respectively, for an initial cell concentration of 140 cells per pattern (Figure 5E). Importantly, we observed many individual cells remaining in solution when generating spheroids with NP1 or NP2 labeled cells, but not with NP3. This suggests that with weakly magnetized cells, the magnetophoretic force is not sufficient to effectively attract all the cells towards the magnets.

Overall, the proposed method for generating magnetic spheroids offers easy handling, fine control over the spheroids size, as well as high-throughput production. Indeed, a micro-patterned glass slide of 75 mm x 26 mm can produce more than 80,000 spheroids and can be easily parallelized.

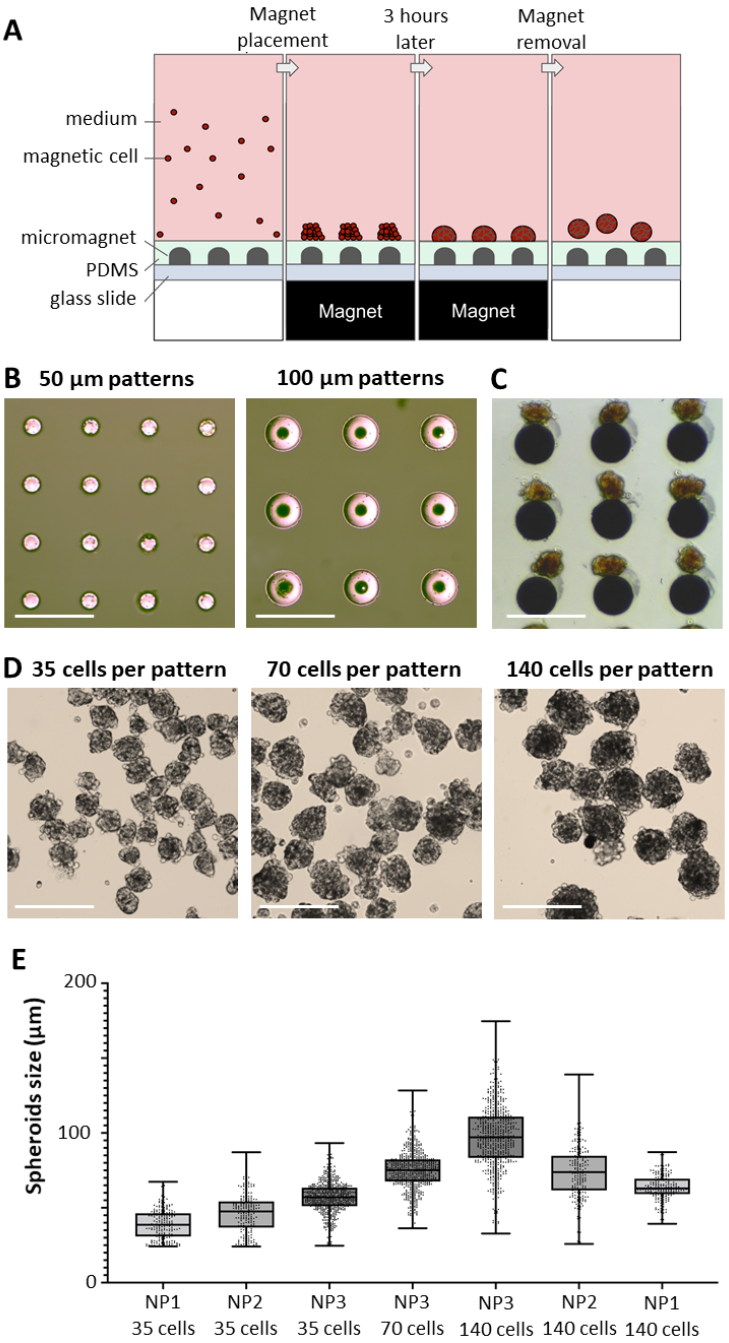

Figure 5. Spheroid production with magnetic micro-patterns. (A): Illustration of the spheroid production process with the magnetic micro-patterns. (B): View from the top of the 50 and 100 µm wide magnetic nickel patterns and (C): view from below the patterns immediately after spheroids were produced and started to move away from the patterns as the magnet was removed. (D): Images of the spheroids produced at a concentration of 35, 70 and 140 cells labeled with NP3 per pattern. Scale bars = 200 µm. (E): Boxplots including all experimental data of the distribution of the spheroids' diameters for these 3 conditions (200 spheroids measured per production, with 3 productions for each condition,) and for spheroids made with cells labeled with NP1 and NP2, for 35 and 140 cells per pattern (200 spheroids measured over one production per condition).

2.6. Alignment of magnetic spheroids

Equipped with many of these highly magnetic spheroids, the next step was to evaluate the ability of our approach to magnetically align them in collagen hydrogel. The magnetic dipolar force exerted by one spheroid on another in contact is in the range of 190, 260, and 350 pN, for spheroids containing 35, 70, and 140 cells, respectively. Each spheroid thus becomes a unique building block, that could be organized within a fiber upon alignment with other spheroids. Here, the average spheroid size obtained ranges from 57 to 97 µm, which is in good agreement with *in vivo* observations of myofibers diameters.[4c, 24]

Figure 6 investigates the optimal experimental conditions to generate spheroid chains for different magnetic labelings, spheroid sizes and spheroid concentrations. Concerning the influence of the magnetic labeling, it clearly appeared that, when using spheroids made of 140 cells, the strong labeling condition (NP3) achieves proper chain formation, but not the weak labeling condition (NP1) that leads to only a few chains made of 2 or 3 spheroids, with many isolated spheroids left (Figure 6A). As for individual cells, an increased magnetization favors alignment. Concerning the impact of the spheroids size on chain formation, Figure 6B illustrates spheroids (NP3 labeling) chaining for spheroids made of 35, 70 and 140 cells (keeping the total number of cells at 1 million per mL). Chain length increases with spheroid size, with an average length of 148±3 µm and 184±6 µm for spheroids made of 35 to 140 cells, respectively. Finally, similarly to individual cells experiments, an increase of spheroid concentration improved on-chip spheroids alignment. By increasing the equivalent cell concentration to 1.5 million cells/mL, an average chain length of 252±11µm was achieved, with the longest chains being up to 1 mm long (Figure 6C, 6E).

Eventually, the possibility to co-culture fibroblasts with the aligned spheroids was evidenced (Figure 6D), the presence of non-magnetic fibroblasts randomly dispersed in the gel having no significant impact on the chain formation and length. Figure 6E summarizes all measurements made on single chains for each condition (over 200 spheroids chains analyzed per condition, and up to 1000, on at least 3 different samples) in the form of boxplots, showing both the median values and the large distribution.

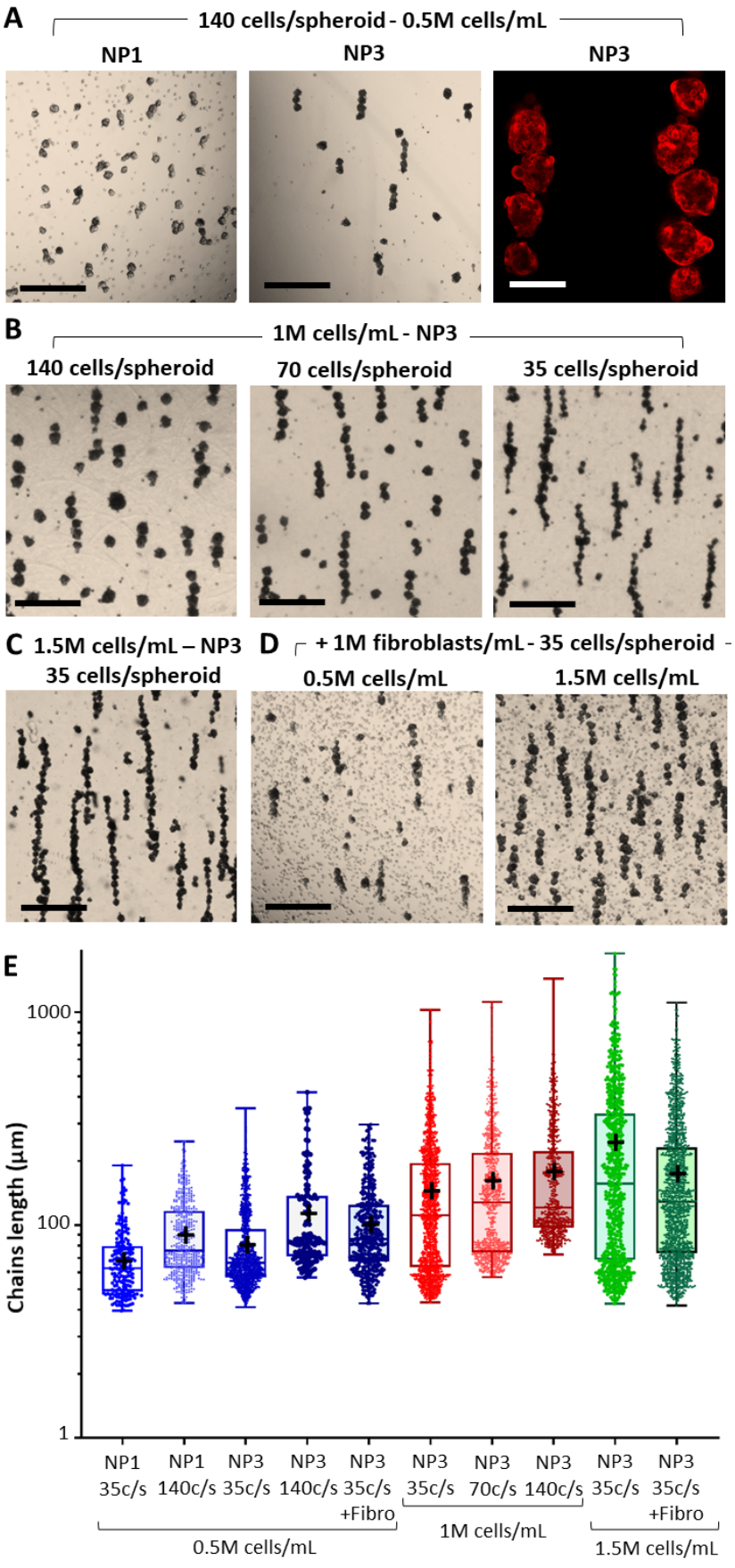

Figure 6. Impact of the magnetic labeling, the spheroid size, and the spheroid concentration on the magnetic spheroid chain length. (A): Images of the alignment of spheroids made with

140 NP1- and NP3-labeled cells per pattern at equivalent concentration of 0.5 million cells per mL, imaged with bright-field and confocal microscopy (using LifeAct transfected cells). (B): Images of the alignment of spheroids made with 35, 70 and 140 NP3-labeled cells at equivalent 1 million cells per mL concentration. (C): Image of alignment of spheroids made with 35 cells at 1.5 million cell per mL equivalent concentration. (D): Images of alignment of spheroids made with 35 NP3-labeled cells in hydrogel with 1 million fibroblasts per mL randomly dispersed fibroblasts at 0.5 and 1.5 million muscle cells per mL equivalent concentration. Scale bars = 500 µm, except for confocal image in (A) with scale bar = 100 µm. (E): Boxplots showing all experimental data points of the chain length distributions for the 8 conditions and for the alignments of spheroids made with 35 NP1- and NP3-labeled cells (over 200 spheroids chains analyzed per condition, and up to 1000, on at least 3 different samples) .

2.7. Spheroid chain fusion and muscle tissue differentiation

Although creating an anisotropic cell organization within a 3D scaffold is crucial for muscle tissue engineering, it is only the first step to eventually generate mature muscle tissue in a 3D microenvironment. So, the chips containing the aligned spheroids in polymerized collagen were filled with differentiation medium to trigger muscle cell differentiation. A LifeAct transfected C2C12 cell line made possible the observation of fluorescent F-actin at both the cell and spheroid level over time. **Figure 7** documents the chains evolution from the day of the alignment (day 0) to one (day 1) and four (day 4) days later. At day 0, just after alignment, the spheroids are distinct from each other and, even though they are aligned they do not seem to interact. However, they fuse one to the other, rapidly, within a few hours. After one day (day 1), all spheroids within the same chain become one, resembling a single elongated ellipsoid (Figure 7A). The persistent shapes of the individual spheroids, that were still present at day 1, were no longer visible at day 4 (Figure 7A-G). This observation was consistent for all conditions: i.e., for chains generated with spheroids of different sizes as well as for different lengths of spheroid chains, from two to ten spheroids per chain (Figure 7A-G). These results demonstrate that the magnetic alignment of spheroids can induce the formation of cohesive cell assembly over time thanks to spheroid fusion within the same chain. Spheroid fusion has been investigated to address fundamental questions about cell self-assembly or tissue organization[25] as well as for tissue engineering purposes.[26] A common method to promote spheroid fusion is most likely the hanging drop method[25a, 27] while an improved control of spheroids fusion can be achieved by an accurate positioning of spheroids within a scaffold.[28] Compared to existing approaches, the magnetic alignment of spheroids within a 3D microenvironment developed here offers new avenues to control general spheroid assembly across a large scale without needing fine control over their positioning.

All chains from all conditions (over 50 chains analyzed per condition) were quantified according to the chains angle (Figure 7H), and aspect ratio (major axis over minor axis of the equivalent ellipse, Figure 7I). The angle reflects the ability of the spheroid chains to keep their anisotropy over time, crucial to favor muscle cell differentiation. Figure 7H clearly demonstrates that all chains maintain their orientation from day 0 to day 4, with yet a notable dispersion of the angle distribution at day 4. Even though chain orientation did not vary over time, the dimensions of the chains, in particular their aspect ratio, did (Figure 7I): the aspect ratio of spheroid chains decreased over time for all spheroid sizes. This can be explained by muscle cells high contractility, especially when they start differentiating. This contraction happens mostly in the direction of the chain main axis, which would be the preferred contractile direction if the cells were to form fibers in that direction. Besides, together with contraction along the chain axis, some cells also escape the chain, resulting in its enlargement. It is worth mentioning that for half the conditions, experiments were carried out by keeping the chips in between the magnets from day 0 to day 4. Nevertheless, the permanent magnetic field did not change neither the chains orientation, nor their aspect ratio, and all data are presented within the same box plot, with black triangles denoting the permanent application of the magnetic field, while red circles correspond to chips outside of the field.

A final functionality of the design of the collagen chips is to combine magnetic alignment with mechanical stretching. A manual stretcher was fabricated (Figure 7J) that accommodate two chips in parallel, allowing to set and keep over time a uniaxial deformation ranging up to 20% (Figure 7J, 7K).[29] The chips were stretched at day 1, and deformation was transmitted to the aligned chains, as illustrated by chains imaging before and after stretching in Figure 7K. 50 chains were analyzed with a resulting average chain elongation of 18.8±6.8%, while the chips themselves suffered a global 20% deformation. The aspect ratio of all chains analyzed are shown in Figure 7L, reproducing the decrease from day 0 to day 1 due to natural muscle cells contractility, but then evidencing a significant increase after stretching.

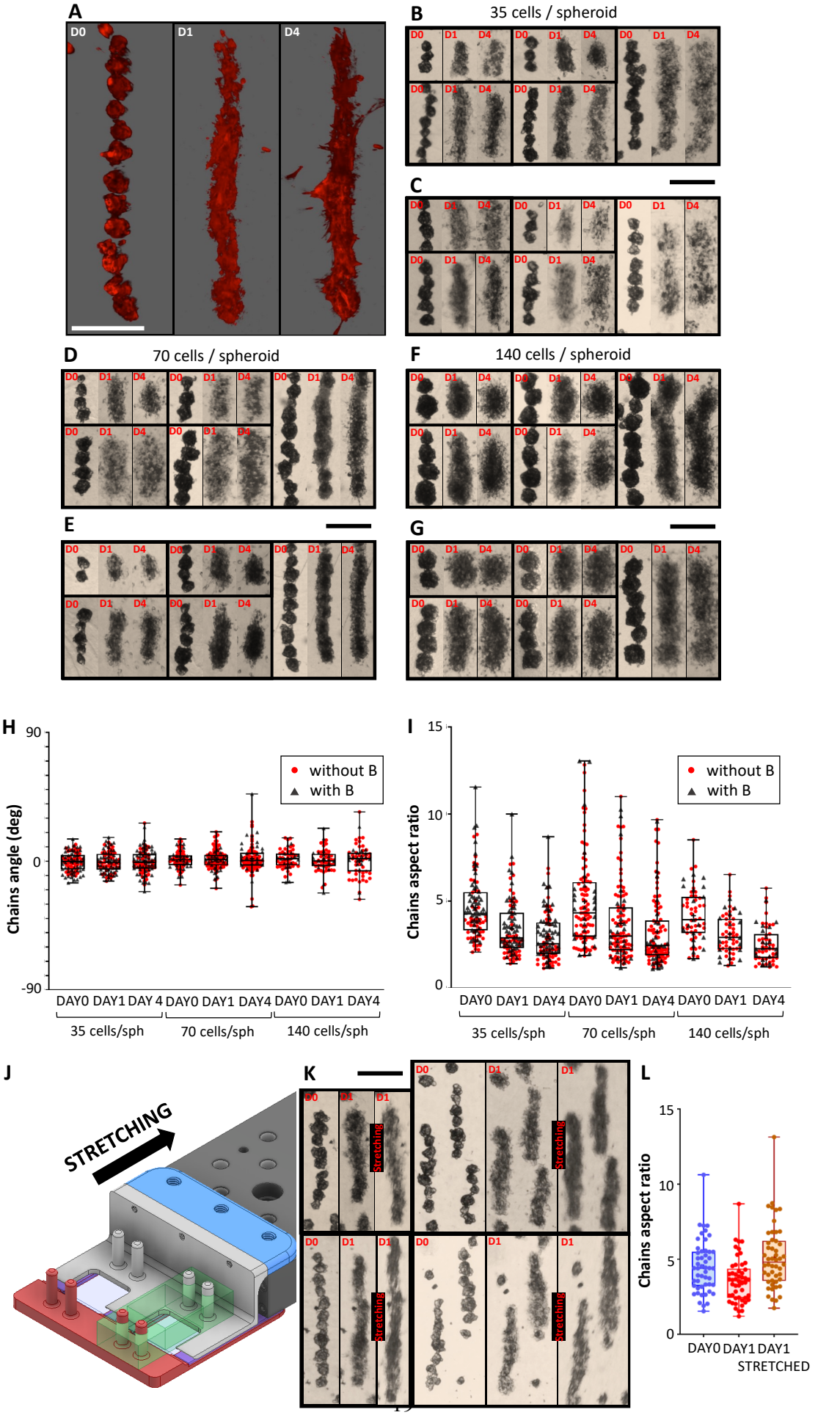
A
D0
D1
D4
B
35 cells / spheroid
C
D
70 cells / spheroid
F
140 cells / spheroid
E
G
H
Chains angle (deg)
90
0
-90
without B
with B
DAY0 DAY1 DAY 4 DAY0 DAY1 DAY4 DAY0 DAY1 DAY4
35 cells/sph
70 cells/sph
140 cells/sph
I
Chains aspect ratio
15
10
5
0
without B
with B
DAY0 DAY1 DAY4 DAY0 DAY1 DAY4 DAY0 DAY1 DAY4
35 cells/sph
70 cells/sph
140 cells/sph
J
STRETCHING
K
Stretching
L
Chains aspect ratio
15
10
5
0
DAY0 DAY1 DAY1
STRETCHED

Figure 7. Evolution of the morphology of the spheroid chains over time. (A): 3D reconstruction from a stack of confocal images of a spheroid chain made with mScarlet LifeAct cells at day 0, day 1 and day 4. (B-G): Images at day 0, day 1 and 4 of the evolution of chains of spheroids made with NP3-labeled cells with 35 cells per spheroid (B,C), 70 cells per spheroid (D,E), 140 cells per spheroid (F,G). Chains in (B,D,F) were removed from the magnets once they were aligned for 30 min, whereas chains in (C,E,G) were between the magnets from day 0 to 4. (H,I): Boxplots of the distributions of the chains angle (H) and aspect ratio (I) for chains of spheroids made with 35, 70 and 140 cells at days 0, 1 and 4, whether or not the chains were kept between magnets at all times (triangles with magnet, circles without magnet, respectively with or without B in the figure). (J): 3D design of a mechanical stretcher to deform the PDMS chips holding the collagen scaffold. (K,L): Images (K) and boxplots (L) of the aspect ratio distribution of spheroid chains at day 0 and day 1 before and after stretching stretching. At least 50 chains were studied for each condition of all graphs. Scale bars = 200 µm.

To further compare these different approaches to developing a skeletal muscle tissue on a chip, the spheroid-based samples were stained for actin and nuclei after 8 days of culture in differentiation medium, and then imaged with confocal microscopy (**Figure 8**). Figure 8A shows a typical chain that clearly formed a 3D tube like assembly after 8 days in differentiation medium. The cell organization within this cylindrical structure showed that in addition to the overall elongation of the structure the cells and their nuclei appear elongated. The actin filaments align along the main direction of the chain. Moreover, several multinucleated cells can be observed confirming that the differentiation process occurs. Figure 8B illustrates a chain that was magnetically aligned at day 0, and then stretched at day 1. Stretching did not notably affect fiber organization. After 8 days of differentiation, the overall structure remained, individual cells were elongated and oriented along the main alignment axis.

Finally, when magnetic spheroids were co-cultured with fibroblasts over the differentiation process (Figure 8C), myofibers were clearly seen, the longest ones being more than 500 µm long. Bright-field microscopy showed the fibers located where the spheroid chain fused, darker in contrast than the non-labeled surrounding fibroblasts. Within these fibers, the nuclei are elongated and mostly located at the cell periphery as observed *in vivo*.[30] Both the myofibers, and the actin filaments within them, are oriented in the direction of the chain. 3D reconstitution of these confocal images finally confirmed that we succeeded in recreating three dimensional muscular fibers. Altogether, these results demonstrate that magnetically aligning spheroids in a 3D hydrogel scaffold without or with co-cultured fibroblasts, allowed generating oriented 3D skeletal muscle fibers.

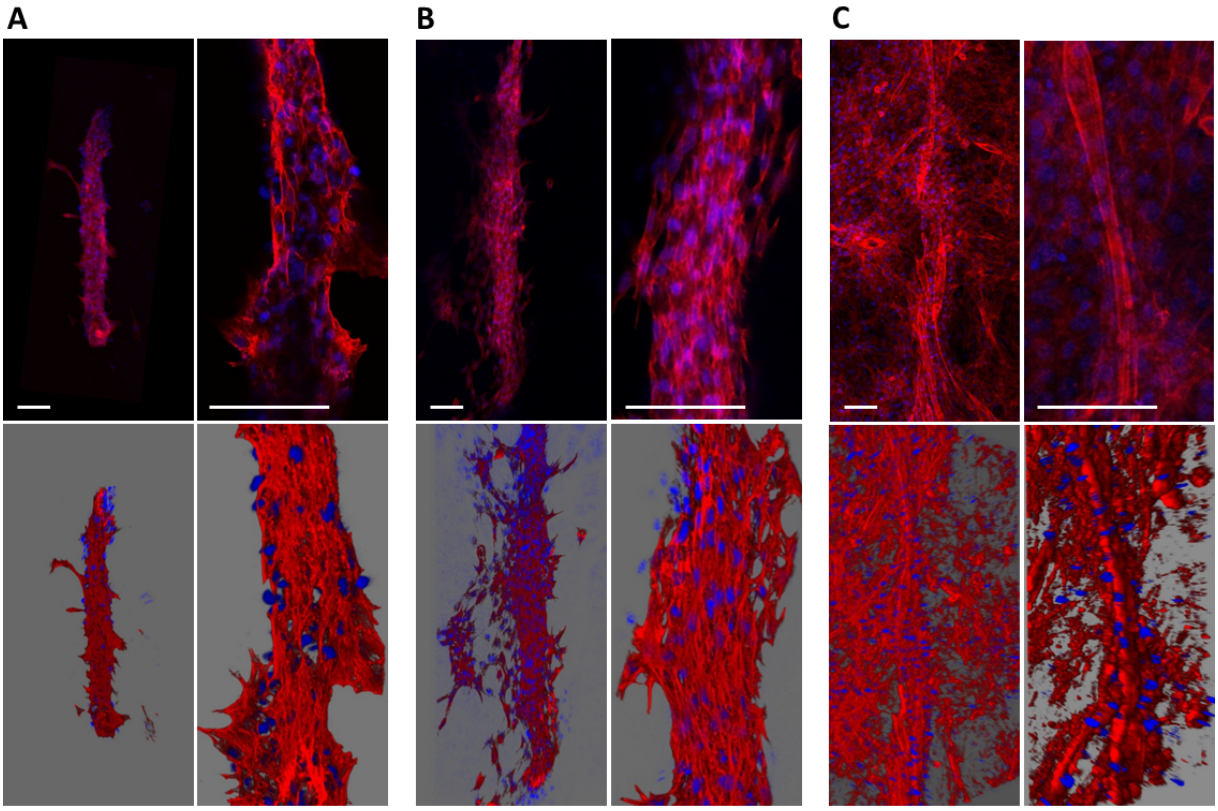

Figure 8. Confocal imaging of spheroid chains after several days of differentiation. Actin was stained in red and nuclei in blue. 2D z-slices (top) and 3D reconstructions from z-stacks (bottom) of spheroid chains: (A) left in differentiation medium (day 7), (B) left in differentiation medium and was stretched at day 1 (day 7) and (C) of a spheroid chain where magnetic muscle cells were co-cultured with 1M/mL fibroblasts (day 5). (Scale bar = 100µm)

2.8. Versatility of the method

Aside from muscle tissue, many living tissues present an anisotropic organization. Therefore, the two-fold magnetic method was applied to two other cell types, to investigate whether it can be a versatile tissue engineering tool (**Figure 9**). It was tested on mice fibroblasts (Fig. 9A), which so far had only been used as non-magnetic cells for co-culture. The fibroblasts were labeled with the NP3 labeling, and were used for making spheroids through magnetic patterning. Spheroids were successfully formed by incubating fibroblasts 3h over the magnetic patterns, with on average 35 cells per pattern. The spheroids were successfully created, with an average diameter of 70 µm. They could then be aligned, and after one day they formed single long fibers, with peripheral cells starting colonizing the gel. The method can therefore be applied to connective tissue, such as tendons and ligaments, that exhibit anisotropic structures as well.[31] The magnetic engineering method was next applied to human mesenchymal stem cells (hTERT) (Figs. 9B and 9C). Spheroids were easily formed by magnetic patterning, starting from 35, 70 and 140 cells per pattern, and leading to spheroids of average diameters of 73, 92, and 107 µm, respectively. Upon magnet application, they

aligned, and formed after one-day well-defined fiber-like structures, that could be further used for the regenerative potential of stem cells.

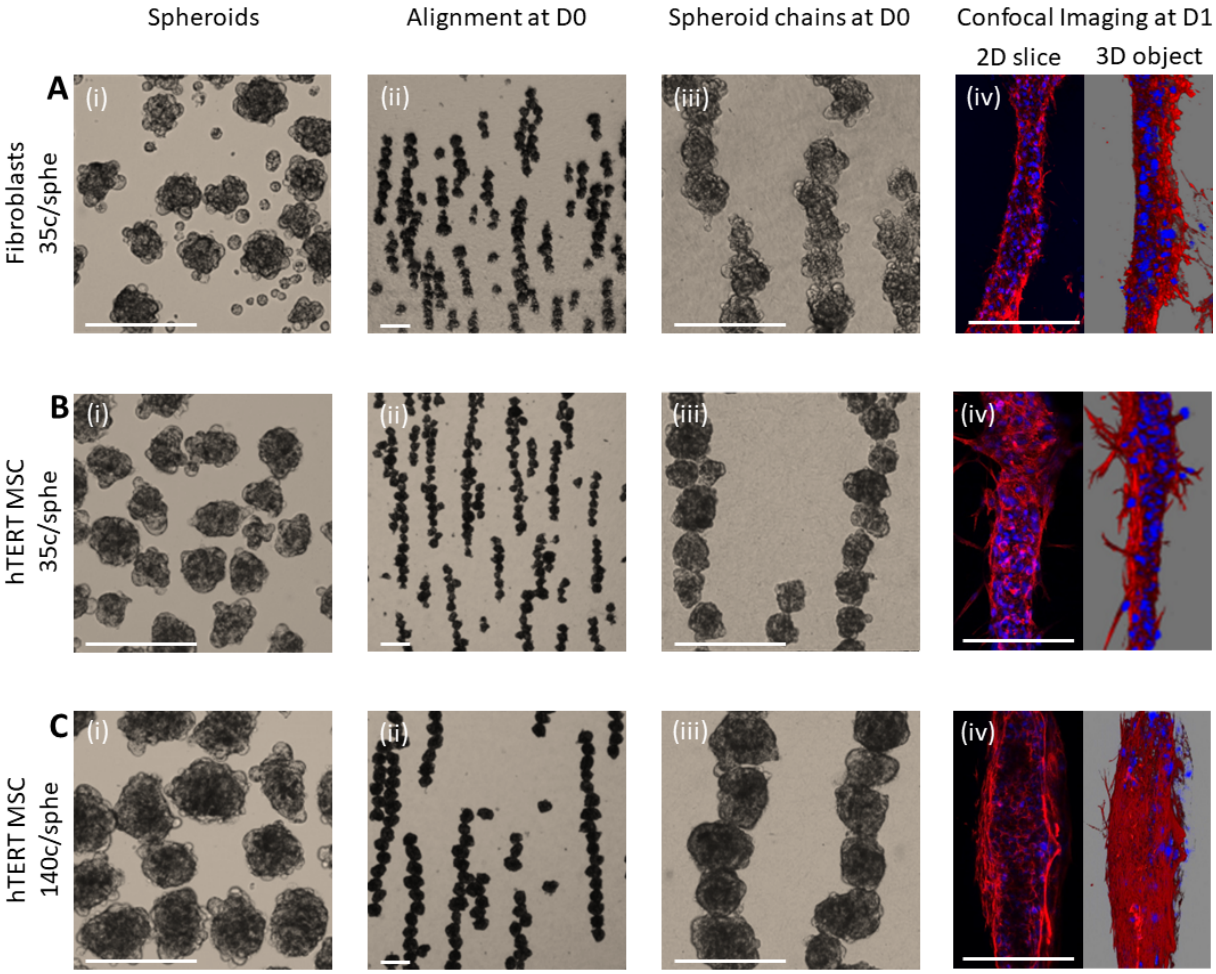

Figure 8. Spheroid making and alignment procedures applied to spheroids with (A) 35 fibroblasts per spheroid, (B) 35 and (C) 140 mesenchymal stem cells (hTERT MSC) per spheroid: (i) spheroids after fabrication; (ii) spheroids chains (close-up in (iii)) just after alignment, and (iv) 2D and 3D confocal imaging of the fiber-like structures created after one-day in DMEM medium supplemented with 2% serum. Scale bar = 200µm.

3. Conclusion

Finding new ways to organize cells in a 3D scaffold with remote forces is beneficial to make tissue engineering progress. When it comes to skeletal muscle tissue, inducing an anisotropic organization is key to induce proper cell differentiation. In this work, two magnetic-based approaches are presented and exploited to develop an innovative approach for tissue engineering and in particular for organ on chip development. The first approach allows to generate at high throughput magnetic spheroids as tissue building blocks, while the second one offers a new way to align magnetic cells or spheroids along a strong uniform magnetic field. Combined, the two-step process enabled the creation of anisotropic muscle fibers

oriented in the magnetic field direction. The magnetic labeling had to be optimized upstream, producing highly magnetic cells, having internalized up to 20 pg of iron per cells, with no impact on cell metabolic activity or capacity to differentiate. With these magnetic cells, the spheroid magnetic patterning technique offers a high yield of spheroid production with a good control over their size. Magnetic cells or spheroids made of dozens of them could then be aligned in 3D in a thermoresponsive collagen gel between two strong magnets specifically positioned at a distance avoiding any magnetic field gradient. Once the gel polymerized, the cells or spheroids were trapped in this anisotropic structure of controlled size. Structures made with aligned spheroids were the only ones that maintained their anisotropy over time, demonstrating the need for building blocks made of tens of cells. Strikingly, in a matter of days, the spheroid chains fused into fiber-like structures. These fibers could also be either 20% stretched one day after their formation or co-cultivated in the 3D collagen gel with randomly dispersed fibroblasts, with several myofibers formed in the direction of the alignment. Differentiation could be further improved by investigating other stretching conditions, complementing differentiation medium with growth factor or even electrical stimulation. Co-culture of neurons could also be studied in order to recapitulate the in vivo architecture of muscle tissue more faithfully. Moreover, we showed that both the magnetic spheroid making and alignment methods can be applied to other cell types, such as fibroblasts and mesenchymal stem cells, where spheroids were easily fused, forming fiber-like structures. Overall, this work demonstrates that combining magnetically assisted 3D strategies with organ on chip technology is beneficial for the fabrication of anisotropic fiber-like tissue engineered constructs, at centimeter scale, with fiber diameter of controlled size in the 10-100 μm range.

4. Experimental Section

Cell culture: Mouse myogenic C2C12 cell line was obtained from ATCC and cells were cultured following conventional procedure in a growth medium made of DMEM (Gibco) supplemented with 10% v/v fetal bovine serum (Thermofisher) and 1% v/v penicillin/streptomycin (Thermofisher). The medium was changed every two days and cells were passed for confluency reaching 50% to 80% using TrypLE dissociation agent (Gibco). In experiments meant to induce cell differentiation, cells were used up to passage 10, otherwise they were used up until passage number 20. hTERT human mesenchymal stem cells (AM-T0523 Immortalized Human Bone Marrow, Euromedex), NIH3T3 fibroblasts (ATCC) were cultured in the same conditions. C2C12 cells with fluorescent actin were

designed by transfecting wild type cells with the plasmid vector pLVX-LifeAct-mScarlet, n°153, 2630 ng/µL. Standard molecular cloning techniques were used to facilitate stable cell line generation by puromycin selection.

Magnetic cell labeling: Iron oxide (maghemite) superparamagnetic nanoparticles were used to magnetically label C2C12 cells. The nanoparticles were produced by iron salts co-precipitation, resulting in an average diameter of 8 nm and a polydispersity index of 0.37 and were coated with citrate ions to preserve their stability in an aqueous solution at pH 7 by electrostatic repulsions. Besides, the negative surface charge (zeta potential = -35 mV) also favors the cellular internalization. They were selected as some of the most used maghemite nanoparticles for biomedical applications.[32] Prior to use, the stock solution of magnetic nanoparticles (2 M of iron) was sterilized by filtration through a 200 nm filter. The magnetic labeling was then performed by incubating the cells with a nanoparticle solution diluted in culture medium RPMI in which 2 mM free citrate was added to avoid nanoparticle precipitation. The pH of the RPMI medium was not affected by the addition of citrate or the nanoparticles. Nanoparticles uptake was tested for different incubation times (from 15 min to 18 hrs) at [Fe]=2 mM, and different iron concentration (from 0.5 to 64 mM) for 30 min duration. Besides, a multi-step incubation was set-up, corresponding to 1, 2, or 3 30 min incubation at [Fe]=2mM. The first labeling condition (one single incubation) was named NP1. The two other labeling conditions, named NP2 and NP3, consisted in performing the NP1 labeling every day for two or three days respectively. All incubations were performed at 37°C, and cells were rinsed afterwards in RPMI and placed back in C2C12 growth medium for at least 1 h prior to any further operations.

Quantification of internalized iron oxide by magnetophoresis: Magnetophoresis was performed to measure the magnetization of the labeled cells, and by extension the amount of internalized iron oxide.[32a] Cells suspended in PBS were placed next to a permanent magnet, generating a field B = 0.145 T and a gradient grad(B) = 17 $T.m^{-1}$. This way, the magnet attracted magnetically labeled cells, and cell migration was imaged through bright-field microscopy. The movies were then analyzed to measure cell radii and velocities, from which the magnetic force was determined by calculating the force balance with respect to Stokes drag law. The mass of iron oxide within cells was then determined from the magnetic moment calculated using the determined cellular magnetic force. For a cell of diameter d and velocity v, the mass of internalized iron is $m_{Fe} = \frac{M(Fe_2)}{M(Fe_2O_3)} \frac{\rho}{M_v} \frac{3\pi\eta dv}{grad(B)}$ with $M(Fe_2)$ and $M(Fe_2O_3)$ the density of magnetic moment of Fe_2 and Fe_2O_3 respectively, M_v the density of magnetic moment of a nanoparticle in a field of 0.145 T, ρ the density of a nanoparticle and η the

viscosity of water. 200 single cell motions were analyzed for each single measurement, and the measure was made in triplicate.

Alamar Blue Metabolic assay: The metabolic activity of the magnetically labeled cells was quantified using the Alamar Blue assay and compared with non-magnetic control cells. The Alamar Blue reagent was incubated (10% in DMEM) with cells cultured in 96-well plate for 1 h (100 µL per well) and was read with a fluorescence plate reader (Enspire, Perkin Elmer) at 570 nm excitation wavelength and 585 nm detection wavelength following the vendor's instructions.

LIVE/DEAD assay: The cytotoxicity of the magnetic labeling was tested using a LIVE/DEAD® cell imaging kit (488/570, Invitrogen). The LIVE/DEAD reagents were incubated with cells in a 24-well plate for 15 min. The wells were then imaged with confocal microscopy with a 488 nm excitation wavelength for the live cells and a 570 nm excitation wavelength for the dead cells. The live cells appeared in green while the dead cells appeared in red, making it possible to count the proportion of dead cells.

Fabrication of the magnetic micro-patterns: The magnetic micro-patterns were fabricated on a glass slide by NiFe electroplating through a photoresist mold.[23] Glass slides (Corning) were cleaned with acetone and isopropanol, after which a Ti-Cu seed layer (Ti 10 nm, Cu 100 nm) was deposited by magnetron sputtering (Plasmionique) to render them electrically conductive. TI-Prime (Microchemicals) was applied as an adhesion promoter, and an epoxy-based negative photoresist (AZ 125nXT, Microchemicals) was spun to a thickness of 70 µm, exposed through a chromium mask and developed, leaving bare copper only where the magnetic patterns were to be grown. NiFe (80:20) deposition was performed by electroplating in a bath containing NiSO4 (250 $g.L^{-1}$), FeSO4 (5 $g.L^{-1}$), boric acid (25 $g.L^{-1}$), saccharin (2 $g.L^{-1}$) and sodium dodecyl sulfate (0.1 $g.L^{-1}$) at 30 °C under magnetic stirring. A current density of 7 $mA.cm^{-2}$ was applied between the substrate and a pure nickel anode (Goodfellow), leading to a growth rate of 4 $\mu m.h^{-1}$. When a thickness of 50 µm was achieved, the photoresist and copper layers were dissolved in TechniStrip P1316 (Technic) at 70 °C. A 100 µm PDMS layer (Sylgard 184, curing agent ratio 1:10 w/w) was then spun on the substrate and cross-linked for 2 hours at 70 °C, after which PDMS wells were bonded using oxygen plasma (Diener Pico) and UV-sterilized.

Magnetic spheroid formation using the magnetic micro-patterns: The wells of the magnetic micro-patterns plate were first treated with an anti-adherence rinsing solution (Stemcell Technologies) for 1 h at room temperature and rinsed with PBS. The wells were filled with differentiation medium into which magnetic cells were suspended, the cell concentration

being adjusted to control the number of cells per magnetic spot. The plate was then placed onto a magnet (110.6 x 89 x 19.6 mm, with remanence Br = 1.35 T, Ref. Q-111-89-20-E, Supermagnete) leading to the aggregation of cells on top of each magnetic spot. After a 3 h incubation at 37 °C, the plate was taken off the magnet, and the so formed spheroids were harvested and resuspended in differentiation medium.

PDMS chips fabrication: Two chip designs were used: a first one for static long-term observation, and a second one for mechanical stretching. Both designs were made of PDMS (Sylgard 184) with a prepolymer/curing agent ratio of either 10:1 w/w for static experiments or 20:1 w/w for stretching experiments to increase elasticity. PDMS chips with a 1 cm deep 2 by 2 cm reservoir with a central well (10 by 7 mm rectangle, 1 mm deep) were fabricated by molding onto custom brass molds prepared by micromilling (Minitech) as described in a previous work.[29] For the static experiments, the PDMS at the bottom of the central wells was cut out and the chips were then plasma bonded on glass coverslips. For mechanical stretching, the PDMS bottom was kept, and additional holes were added to the sides of the chips, which were then clamped onto a custom mechanical stretcher based on a manual translation stage (Thorlabs). All the chips were then subjected to an APTES (3-Aminopropyl)triethoxysilane (Sigma-Aldrich) and Glutaraldehyde (Sigma-Aldrich) treatment to promote covalent anchoring of collagen to PDMS as described previously.[33] The PDMS chips were then UV-sterilized immediately prior to cell and hydrogel scaffold seeding.

Seeding of cells or spheroids in PDMS chips with collagen/matrigel scaffold: A hydrogel scaffold solution was prepared at 4 °C, containing 2 $mg.mL^{-1}$ of rat tail collagen type I (Corning, stock pre equilibrated at pH 7 with NaOH), 10% v/v of matrigel matrix (Corning), 1× PBS, and 40% v/v of differentiation medium. The hydrogel scaffold solution was then mixed with cells or spheroids before being seeded in PDMS chips and left to polymerize for 30 min in an incubator at 37 °C.

Cell differentiation: To promote cell differentiation after seeding in the collagen/matrigel scaffold, a differentiation culture medium made of DMEM (Gibco) containing 1% v/v horse serum (Thermofisher) and 1% v/v penicillin/streptomycin (Thermofisher) was used.

Magnetic alignment of cells or spheroids: After seeding the cells (or spheroids) mixed with the cold hydrogel scaffold solution in the PDMS wells, the chips were quickly placed between two iron boron magnets (110.6 x 89 x 19.6 mm, with remanence Br = 1.35 T, Ref. Q-111-89-20-E, Supermagnete) in an incubator at 37°C. Between the magnets, the labeled cells acquire a magnetic moment and align due to the dipole-dipole force, while the 37°C temperature initiates the collagen and matrigel polymerization around the aligned biological objects. The

magnets were kept 3.6 cm apart (although 10 and 8 cm were also tested in **Figure 2**) using custom aluminum parts machined by Protolabs. COMSOL Multiphysics (Magnetic Field No Currents module) simulations were performed to determine the optimal distance between magnets to minimize the magnetic field gradient while keeping a high field intensity.

Fluorescent cell staining: Prior to staining, the culture medium was removed, and the chips were incubated in 4% PFA v/v in PBS for one hour at room temperature to perform cell fixation and washed 3 times with PBS. Collagen samples were detached from the chips and left an hour at 4°C in a blocking solution composed of 4% w/w BSA (Sigma) and 0.5% v/v Triton X-100 (Fisher) in PBS. The samples were rinsed 3 times with PBS. Each sample was then left overnight in 2mL of staining solution (blocking solution with 1:1000 of Thermofisher Phalloidin AlexaFluor 488 and 1:300 Invitrogen DAPI) at 4°C for protein staining. The next day, the samples were rinsed 2 times with PBS at room temperature. The chips were stored in PBS at 4°C until imaged.

Confocal imaging: Samples were imaged using a Leica DMi8 inverted confocal microscope. Either a 10X air objective or a 25X water immersion objective were used. Collagen samples were placed using tweezers onto a fluorodish and laid flat for imaging.

Perls staining of intracellular iron: Perls' Prussian blue staining reveals iron within labeled cells in blue. The cells were fixed as was done for confocal imaging. They were then further stained for 5 min using 0.5 g of potassium hexacyanoferrate (II) (Sigma) dissolved in 10 mL of distilled water mixed with 10 mL of Hydrochloric Acid 1N (Fisher Chemical). Counterstaining was next performed using 0.5 g of Nuclear Faster Red (Fisher Chemical) together 10 g of Aluminum sulfate hydrate dissolved in 200 mL of demineralized water.

Transmission electron microscopy imaging: Cells were fixed for an hour in a solution made of 0.1 mol/L sodium cacodylate buffer (Sigma-Aldrich) supplemented with 5% glutaraldehyde. Rinsing (two times) was performed in 0.1 mol/L sodium cacodylate buffer, and samples were then contrasted with 0.5% Oolong Tea Extract (OTE), after that postfixed with 1% osmium tetroxide, and finally embedded in epoxy resins. Ultrathin slices (70 nm) were sectioned, counterstained with lead citrate, and imaging was achieved with a Hitachi HT 7700 at 80 kV (INRAE, UMR 1313 GABI, MIMA2-Plateau de Microscopie Electronique, 78352 Jouy-en-Josas, France).

Statistial Analysis: Magnetophoresis measures were performed on 200 cells per experiment, with 3 experiments per condition, by measuring their speed and diameter using Fiji. Results were presented in Figure 1 as mean ± standard deviation.

Evolution of the angle distribution after individual cell alignment was measured using Fiji's OrientationJ plugin on three different samples for each condition.
Chains and spheroids' sizes, elongation and angle were obtained with Fiji's Analyze particles module.
Spheroid sizes were measured over 3 productions for the NP3 labeled conditions and 1 production for the other conditions, with 200 spheroids measured per production.
Chain lengths were measured over 3 different samples per condition, with overall at least 2000 chains measured for individual cell chains, and overall 200 to 1000 chains measured for spheroid chains. As the size and the number of objects aligned changes not only the length of the chains but also the overall number of chains in one sample, not all conditions have the same number of chains per sample. For the spheroid chains, all the chains of each sample were measured, but some only have 200 while others have more than 1000.
Chains' elongations and angle throughout time were measured on at least 50 different chains per condition.
Statistical representations were performed using GraphPad Prism 8 (GraphPad Software, La Jolla, California).

Acknowledgements

This work was supported by the French Agence nationale de la recherche (ANR) under grant ANR-19-CE09-0029, Myochip H2020 FET OPEN project. This work has received the support of "Institut Pierre-Gilles de Gennes" (laboratoire d'excellence, Equipex, "Investissements d'avenir" program ANR-10-IDEX-0001-02 PSL and ANR-10-LABX-31-34). We thank Chrsistine Péchoux from INRAE, MIMA-2, Jouy en Josas, for TEM imaging. We thank Pierre Burckel, from the platform quadrupole ICP-MS at Institut de Physique du Globe de Paris for ICP measurements. ICP-MS analyses were supported by IPGP multidisciplinary program PARI and Paris–IdF region SESAME Grant no. 12015908. We thank David Hrabovsky from the platform from the MPBT platform at Sorbonne University, for VSM measurements. We thank Fanny Cayrac, from BMBC platform (UMR168, Curie Institute) for designing fluorescent muscle cells, and we also thank Fahima Di Federico from BMBC platform for discussions. We thank Laurianne Gérémie for help with the stretched PDMS chips technology. We are grateful to Aurore Van de Walle, Jose Efrain Perez and Amanda Silva for fruitful discussions.

Received: ((will be filled in by the editorial staff))
Revised: ((will be filled in by the editorial staff))
Published online: ((will be filled in by the editorial staff))

Table of contents entry

Spheroids are created by attracting magnetic muscle cells to micromagnets. They are next aligned in a 3D thermoresponsive collagen hydrogel between two strong magnets. As the gel polymerizes around the spheroids chains, they are trapped in an anisotropic organization. After differentiating for a couple of days, the spheroids fuse into 3D fiber-like muscle structures.

N. Demri, S. Dumas, M. Nguyen, G. Gropplero, A. Abou-Hassan, S. Descroix*, C. Wilhelm*

Remote magnetic microengineering and alignment of spheroids into 3D cellular fibers

ToC figure (55 mm broad × 50 mm high)

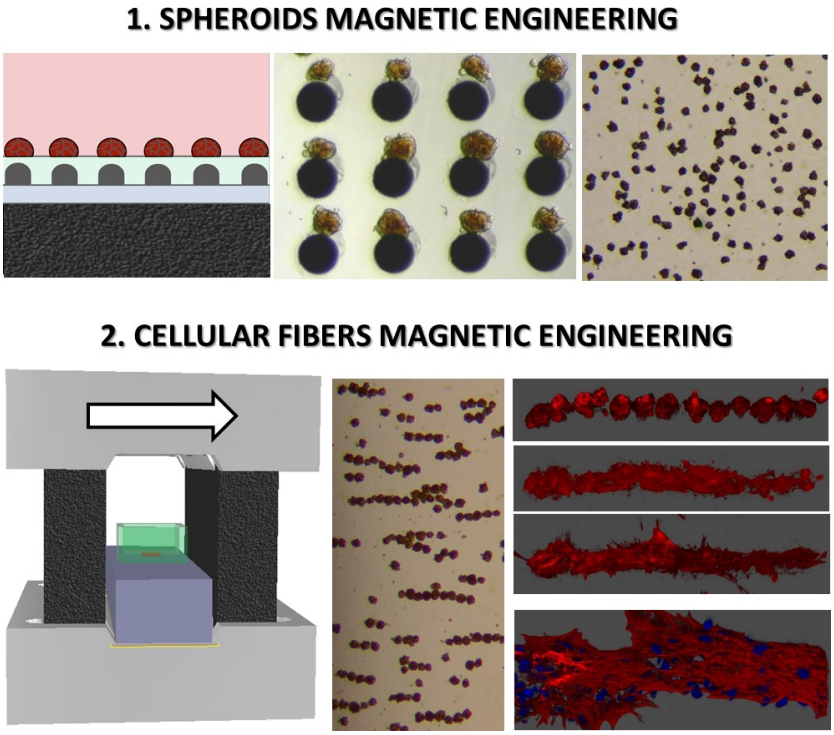

References

[1] B. Zhang, A. Korolj, B. F. L. Lai, M. Radisic, *Nature Reviews Materials* **2018**, 3, 257.

[2] a) D. E. Ingber, *Nature Reviews Genetics* **2022**, 1; b) L. A. Low, C. Mummery, B. R. Berridge, C. P. Austin, D. A. Tagle, *Nature Reviews Drug Discovery* **2021**, 20, 345; c) C. A. Paggi, L. M. Teixeira, S. Le Gac, M. Karperien, *Nature Reviews Rheumatology* **2022**, 1; d) I. Matthiesen, D. Voulgaris, P. Nikolakopoulou, T. E. Winkler, A. Herland, *Small* **2021**, 17, 2101785; e) M. Nikolaev, O. Mitrofanova, N. Broguiere, S. Geraldo, D. Dutta, Y. Tabata, B. Elci, N. Brandenberg, I. Kolotuev, N. Gjorevski, *Nature* **2020**, 585, 574; f) L. J. Y. Ong, T. Ching, L. H. Chong, S. Arora, H. Li, M. Hashimoto, R. DasGupta, P. K. Yuen, Y.-C. Toh, *Lab on a Chip* **2019**, 19, 2178; g) C. A. Paggi, **2022**.

[3] a) A. G. Kléber, Y. Rudy, *Physiological reviews* **2004**, 84, 431; b) R. L. Lieber, *Skeletal muscle structure, function, and plasticity*, Lippincott Williams & Wilkins, **2002**; c) M. Ghovvati, M. Kharaziha, R. Ardehali, N. Annabi, *Advanced Healthcare Materials* **2022**, 2200055; d) J. R. Soucy, J. Askaryan, D. Diaz, A. N. Koppes, N. Annabi, R. A. Koppes, *Biofabrication* **2019**, 12, 015014; e) K. S. Koeck, S. Salehi, M. Humenik, T. Scheibel, *Advanced Functional Materials* **2022**, 32, 2112238; f) M. Ebrahimi, S. Ostrovidov, S. Salehi, S. B. Kim, H. Bae, A. Khademhosseini, *Journal of tissue engineering and regenerative medicine* **2018**, 12, 2151.

[4] a) S. Ostrovidov, V. Hosseini, S. Ahadian, T. Fujie, S. P. Parthiban, M. Ramalingam, H. Bae, H. Kaji, A. Khademhosseini, *Tissue Engineering Part B: Reviews* **2014**, 20, 403; b) N. Takeda, K. Tamura, R. Mineguchi, Y. Ishikawa, Y. Haraguchi, T. Shimizu, Y. Hara, *Journal of Artificial Organs* **2016**, 19, 141; c) D. Neal, M. S. Sakar, L.-L. S. Ong, H. H. Asada, *Lab on a Chip* **2014**, 14, 1907.

[5] a) H. N. Kim, A. Jiao, N. S. Hwang, M. S. Kim, D.-H. Kim, K.-Y. Suh, *Advanced drug delivery reviews* **2013**, 65, 536; b) H. Takahashi, T. Shimizu, M. Nakayama, M. Yamato, T. Okano, *Biomaterials* **2013**, 34, 7372; c) K. O. Okeyo, Y. Kibe, T. Adachi, *Materials Today Advances* **2021**, 12, 100194.

[6] a) X. He, Q. Xiao, C. Lu, Y. Wang, X. Zhang, J. Zhao, W. Zhang, X. Zhang, Y. Deng, *Biomacromolecules* **2014**, 15, 618; b) A. Hadipour, V. Bayati, M. Rashno, M. Orazizadeh, *Cell Journal (Yakhteh)* **2021**, 23, 603; c) A. Jain, M. Behera, V. Ravi, S. Mishra, N. R. Sundaresan, K. Chatterjee, *Nanomedicine: Nanotechnology, Biology and Medicine* **2021**, 32, 102341.

[7] a) T. Fujie, S. Ahadian, H. Liu, H. Chang, S. Ostrovidov, H. Wu, H. Bae, K. Nakajima, H. Kaji, A. Khademhosseini, *Nano letters* **2013**, 13, 3185; b) K. Y. Vajanthri, R. K. Sidu, S. Poddar, A. K. Singh, S. K. Mahto, *Cytoskeleton* **2019**, 76, 269.

[8] a) W. Bian, B. Liau, N. Badie, N. Bursac, *Nature protocols* **2009**, 4, 1522; b) M. Juhas, G. C. Engelmayr, A. N. Fontanella, G. M. Palmer, N. Bursac, *Proceedings of the National Academy of Sciences* **2014**, 111, 5508; c) N. Rose, S. Sonam, T. Nguyen, G. Grenci, A. Bigot, A. Muchir, B. Ladoux, F. Le Grand, L. Trichet, *bioRxiv* **2021**; d) A. D. Hofemeier, T. Limon, T. M. Muenker, B. Wallmeyer, A. Jurado, M. E. Afshar, M. Ebrahimi, R. Tsukanov, N. Oleksiievets, J. Enderlein, *Elife* **2021**, 10, e60145; e) M. E. Afshar, H. Y. Abraha, M. A. Bakooshli, S. Davoudi, N. Thavandiran, K. Tung, H. Ahn, H. J. Ginsberg, P. W. Zandstra, P. M. Gilbert, *Scientific reports* **2020**, 10, 1; f) B. Xu, M. Zhang, R. C. Perlingeiro, W. Shen, *Advanced Biosystems* **2019**, 3, 1900005; g) K. Yoshioka, A. Ito, M. Arifuzzaman, T. Yoshigai, F. Fan, K.-i. Sato, K. Shimizu, Y. Kawabe, M. Kamihira, *Journal of bioscience and bioengineering* **2021**, 131, 434.

[9] a) S. Cabana, A. Curcio, A. Michel, C. Wilhelm, A. Abou-Hassan, *Nanomaterials* **2020**, 10, 1548; b) I. Rubia-Rodríguez, A. Santana-Otero, S. Spassov, E. Tombácz, C. Johansson, P. De La Presa, F. J. Teran, M. del Puerto Morales, S. Veintemillas-Verdaguer, N. T. Thanh, *Materials* **2021**, 14, 706; c) H. Yan, W. Shang, X. Sun, L. Zhao, J. Wang, Z. Xiong, J. Yuan, R. Zhang, Q. Huang, K. Wang, *Advanced Functional Materials* **2018**, 28, 1705710; d) H. Huang, J. F. Lovell, *Advanced functional materials* **2017**, 27, 1603524.

[10] a) R. P. Friedrich, I. Cicha, C. Alexiou, *Nanomaterials* **2021**, 11, 2337; b) A. Van de Walle, J. E. Perez, A. Abou-Hassan, M. Hémadi, N. Luciani, C. Wilhelm, *Materials Today Nano* **2020**, 11, 100084.

[11] a) A. Ito, K. Ino, M. Hayashida, T. Kobayashi, H. Matsunuma, H. Kagami, M. Ueda, H. Honda, *Tissue engineering* **2005**, 11, 1553; b) T. Kito, R. Shibata, M. Ishii, H. Suzuki, T. Himeno, Y. Kataoka, Y. Yamamura, T. Yamamoto, N. Nishio, S. Ito, *Scientific reports* **2013**, 3, 1; c) A. I. Gonçalves, M. T. Rodrigues, M. E. Gomes, *Acta biomaterialia* **2017**, 63, 110.

[12] G. R. Souza, J. R. Molina, R. M. Raphael, M. G. Ozawa, D. J. Stark, C. S. Levin, L. F. Bronk, J. S. Ananta, J. Mandelin, M.-M. Georgescu, *Nature nanotechnology* **2010**, 5, 291.

[13] a) J. E. Perez, I. Nagle, C. Wilhelm, *Biofabrication* **2020**, 13, 015018; b) L. Labusca, D. D. Herea, A. E. Minuti, C. Stavila, C. Danceanu, M. Grigoras, G. Ababei, H. Chiriac, N. Lupu, *Journal of Biomedical Materials Research Part B: Applied Biomaterials* **2021**, 109, 630; c) E. V. Koudan, M. N. Zharkov, M. V. Gerasimov, S. S. Karshieva, A. D. Shirshova, V. V. Chrishtop, V. A. Kasyanov, A. A. Levin, V. A. Parfenov, P. A. Karalkin, *ACS Biomaterials Science & Engineering* **2021**, 7, 5206.

[14] a) D. Fayol, G. Frasca, C. Le Visage, F. Gazeau, N. Luciani, C. Wilhelm, *Advanced Materials* **2013**, 25, 2611; b) V. A. Parfenov, Y. D. Khesuani, S. V. Petrov, P. A. Karalkin, E. V. Koudan, E. K. Nezhurina, F. D. Pereira, A. A. Krokhmal, A. A. Gryadunova, E. A. Bulanova, V. Mironov, *Science advances* **2020**, 6, eaba4174; c) M. Arifuzzaman, A. Ito, K. Ikeda, Y. Kawabe, M. Kamihira, *Tissue Engineering Part A* **2019**, 25, 563; d) L. Zwi-Dantsis, B. Wang, C. Marijon, S. Zonetti, A. Ferrini, L. Massi, D. J. Stuckey, C. M. Terracciano, M. M. Stevens, *Advanced Materials* **2020**, 32, 1904598; e) G. Yang, F. Jiang, Y. Lu, S. Lin, C. Liu, A. Li, D. L. Kaplan, S. Zhang, Y. He, C. Huang, *Biofabrication* **2021**, 13, 035040.

[15] a) G. Mary, A. Van de Walle, J. E. Perez, T. Ukai, T. Maekawa, N. Luciani, C. Wilhelm, *Advanced Functional Materials* **2020**, 30, 2002541; b) A. F. Almeida, A. Vinhas, A. I. Gonçalves, M. S. Miranda, M. T. Rodrigues, M. E. Gomes, *Journal of Materials Chemistry B* **2021**, 9, 1259; c) Y. Kim, H. Choi, J. E. Shin, G. Bae, R. Thangam, H. Kang, *View* **2020**, 1, 20200029.

[16] a) K. Ishihara, K. Nakayama, S. Akieda, S. Matsuda, Y. Iwamoto, *Journal of orthopaedic surgery and research* **2014**, 9, 1; b) C. Norotte, F. S. Marga, L. E. Niklason, G. Forgacs, *Biomaterials* **2009**, 30, 5910; c) J.-S. Lee, S. Chae, D. Yoon, D. Yoon, W. Chun, G. H. Kim, *Biofabrication* **2020**, 12, 045028; d) K. Zhang, X. Bai, Z. Yuan, X. Cao, X. Jiao, Y. Qin, Y. Wen, X. Zhang, *ACS Applied Materials & Interfaces* **2020**, 12, 7931; e) L. Carr, M. Golzio, R. Orlacchio, G. Alberola, J. Kolosnjaj-Tabi, P. Leveque, D. Arnaud-Cormos, M.-P. Rols, *Bioelectrochemistry* **2021**, 141, 107839; f) Q. Li, G. Qi, X. Liu, J. Bai, J. Zhao, G. Tang, Y. S. Zhang, R. Chen-Tsai, M. Zhang, D. Wang, *Advanced Functional Materials* **2021**, 31, 2104046.

[17] a) X. Zhang, Y. Liu, Q. Zuo, Q. Wang, Z. Li, K. Yan, T. Yuan, Y. Zhang, K. Shen, R. Xie, *International journal of bioprinting* **2021**, 7; b) S. Chae, J. Hong, H. Hwangbo, G. Kim, *Theranostics* **2021**, 11, 6818; c) W. Sun, B. Starly, A. C. Daly, J. A. Burdick, J. Groll, G. Skeldon, W. Shu, Y. Sakai, M. Shinohara, M. Nishikawa, *Biofabrication*

2020, 12, 022002; d) S. M. Hull, C. D. Lindsay, L. G. Brunel, D. J. Shiwarski, J. W. Tashman, J. G. Roth, D. Myung, A. W. Feinberg, S. C. Heilshorn, *Advanced Functional Materials* **2021**, 31, 2007983.

[18] J. Xing, N. Liu, N. Xu, W. Chen, D. Xing, *Advanced Functional Materials* **2021**, 2110676.

[19] a) A. Van de Walle, J. Kolosnjaj-Tabi, Y. Lalatonne, C. Wilhelm, *Accounts of Chemical Research* **2020**, 53, 2212; b) A. P. Sangnier, A. B. Van de Walle, A. Curcio, R. Le Borgne, L. Motte, Y. Lalatonne, C. Wilhelm, *Nanoscale* **2019**, 11, 16488; c) A. Van de Walle, A. Fromain, A. P. Sangnier, A. Curcio, L. Lenglet, L. Motte, Y. Lalatonne, C. Wilhelm, *Nano Research* **2020**, 13, 467.

[20] J. Chal, O. Pourquié, *Development* **2017**, 144, 2104.

[21] a) M. A. Chapman, R. Meza, R. L. Lieber, *Differentiation* **2016**, 92, 108; b) S. J. Mathew, J. M. Hansen, A. J. Merrell, M. M. Murphy, J. A. Lawson, D. A. Hutcheson, M. S. Hansen, M. Angus-Hill, G. Kardon, *Development* **2011**, 138, 371.

[22] a) S. Raghavan, P. Mehta, E. N. Horst, M. R. Ward, K. R. Rowley, G. Mehta, *Oncotarget* **2016**, 7, 16948; b) D. Liu, S. Chen, M. Win Naing, *Biotechnology and Bioengineering* **2021**, 118, 542; c) J. A. Kim, J.-H. Choi, M. Kim, W. J. Rhee, B. Son, H.-K. Jung, T. H. Park, *Biomaterials* **2013**, 34, 8555; d) B. R. Whatley, X. Li, N. Zhang, X. Wen, *Journal of biomedical materials research Part A* **2014**, 102, 1537.

[23] P. Tseng, J. W. Judy, D. Di Carlo, *Nature methods* **2012**, 9, 1113.

[24] S. Gollapudi, J. Michael, M. Chandra, **2014**.

[25] a) N. V. Kosheleva, Y. M. Efremov, B. S. Shavkuta, I. M. Zurina, D. Zhang, Y. Zhang, N. V. Minaev, A. A. Gorkun, S. Wei, A. I. Shpichka, *Scientific reports* **2020**, 10, 1; b) G. Beaune, L. Sinkkonen, D. Gonzalez-Rodriguez, J. V. Timonen, F. Brochard-Wyart, *Langmuir* **2022**, 38, 5296.

[26] A.-C. Tsai, Y. Liu, X. Yuan, T. Ma, *Tissue Engineering Part A* **2015**, 21, 1705.

[27] H. Cui, X. Wang, J. Wesslowski, T. Tronser, J. Rosenbauer, A. Schug, G. Davidson, A. A. Popova, P. A. Levkin, *Advanced materials* **2021**, 33, 2006434.

[28] A. C. Daly, M. D. Davidson, J. A. Burdick, *Nature communications* **2021**, 12, 1.

[29] L. Gérémie, E. Ilker, M. Bernheim-Dennery, C. Cavaniol, J.-L. Viovy, D. M. Vignjevic, J.-F. Joanny, S. Descroix, *Physical Review Research* **2022**, 4, 023032.

[30] W. Roman, E. R. Gomes, presented at Seminars in cell & developmental biology **2018**.

[31] a) R. Vilarta, B. D. C. Vidal, *Matrix* **1989**, 9, 55; b) J. Zhao, X. Wang, J. Han, Y. Yu, F. Chen, J. Yao, *Frontiers in Bioengineering and Biotechnology* **2021**, 9.

[32] a) D. Fayol, N. Luciani, L. Lartigue, F. Gazeau, C. Wilhelm, *Advanced healthcare materials* **2013**, 2, 313; b) M.-S. Martina, V. Nicolas, C. Wilhelm, C. Ménager, G. Barratt, S. Lesieur, *Biomaterials* **2007**, 28, 4143; c) J. E. Perez, F. Fage, D. Pereira, A. Abou-Hassan, S. Asnacios, A. Asnacios, C. Wilhelm, *Journal of Nanobiotechnology* **2021**, 19, 1.

[33] Y. J. Chuah, S. Kuddannaya, M. H. A. Lee, Y. Zhang, Y. Kang, *Biomaterials science* **2015**, 3, 383.